Solid Freeform Fabrication 2023: Proceedings of the 34th Annual International Solid Freeform Fabrication Symposium – An Additive Manufacturing Conference
Reviewed Paper

PROCESS MODELING OF MULTI-MATERIAL LASER POWDER BED FUSION

J. C. Griffis[1], K. S. Shahed[1], C. E. Okwudire[2], G. P. Manogharan[1]

[1]Department of Mechanical Engineering, Pennsylvania State University, State College, Pa
[2]Department of Mechanical Engineering, University of Michigan, Ann Arbor, MI

Abstract

Thermomechanical simulation of the laser powder bed fusion process has been a valuable tool to help researchers and practitioners across the AM production cycle. For instance: Design for AM (DfAM), material development, process mapping, prediction, and support generations, among others. In this study, multi-material laser powder bed fusion (MM-LPBF), specifically of 904LSS and CuSn10 are examined through process simulation and non-destructive techniques to determine the impact of component orientation on defect mitigation. It is determined that material orientation along the build direction is a large contributor in as-build defects. Introductory MM-LPBF simulation is established to better understand the capabilities of current LPBF simulation tools in accurately predicting and mitigating the new challenges of MM-LPBF simulation.

Introduction

The advent of multi-material additive manufacturing (MM AM) is revolutionizing the manufacturing industry in offering unprecedented design freedom and the ability to fabricate complex structures with spatially graded materials. Among AM techniques, laser powder bed fusion (LPBF) has gained significant attention due to its capability to produce components of high resolution and good surface finish [1]. While LPBF has been extensively studied for single-material applications, the exploration of multi-material LPBF is an area of growing interest, as it opens up new possibilities for advanced component fabrication. This study aims to introduce thermally induced strain simulation of multi-material LPBF, focusing on key aspects such as material orientation, process optimization, and interfacial behavior.

904L stainless steel and CuSn10 bronze multi-material components combine strength and stiffness with high corrosive resistance, and high conduction [2]. While this combination yields the pairing to heat exchanger or highly corrosive naval applications, stainless steel and copper have proven to be difficult to manufacturing simultaneously from a materials and manufacturing engineering standpoint due to their difference in thermal expansion coefficients.

The successful implementation of multi-material LPBF heavily relies on the careful selection of compatible materials. Several studies have investigated the compatibility of different material combinations in terms of thermal properties, melting points, and intermetallic reactions. For instance, Tan et al. explored the combination of stainless steel and copper in LPBF, highlighting the challenges related to the large difference in their thermal conductivities [3]. Through thermomechanical simulations, they demonstrated the importance of process parameter selection to mitigate thermal gradients and prevent defects.

Optimizing the process parameters for multi-material LPBF is crucial to achieve desirable material interfaces and avoid defects such as delamination, cracking, and lack of fusion. Numerical simulations play a vital role in understanding the complex thermal and mechanical interactions during the process. Chen et al. investigated the effect of laser power and scanning speed on the

formation of interfacial defects in multi-material LPBF [4]. Their findings emphasized the need for parameter optimization to control the heat transfer and stress distribution at material interfaces. Due to the timely and expensive experimental methods commonly used to identify acceptable process parameters for single material LPBF builds, turning towards numerical simulations for preliminary guidance in material-specific parameter development in the case of MM-LPBF.

This paper aims to present an introductory approach to thermomechanical simulation of MM-LPBF to determine whether the order of material placement along the build direction has a significant impact on the defects occurring at the fusion plane. To investigate this, pairs of witness coupons of opposite material gradients were fabricated and examined using microcomputed tomography (micro-CT) and thermally induced strain simulation. It was determined that component orientation, or material arrangement along the build direction, does have a significant impact on defect occurrences near the fusion plane.

Methods

Build Parameters

Four 1 cm^3 witness coupons were printed with respect to two build and material orientations to identify and evaluate the influence of build orientation in the selective material deposition and sintering process. These orientations sintered 904L stainless steel on top of CuSn10 bronze and vice-versa with the fusion plane parallel to the build plate and are shown in Figure 1.

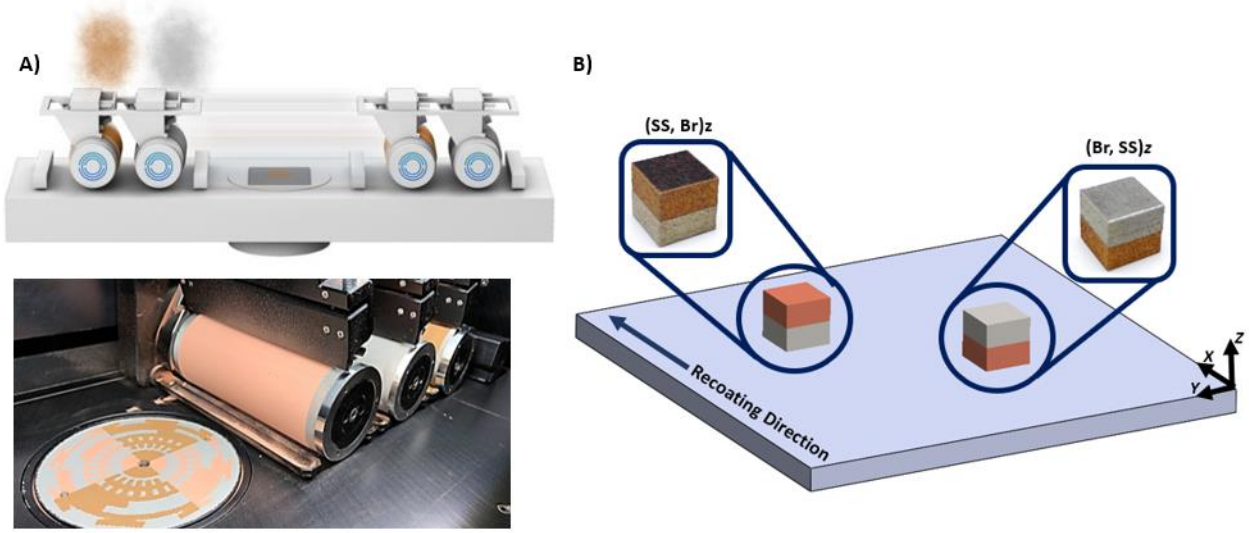

Figure 1: A) Selective Powder Deposition (SPD) recoating chambers for multi-material LPBF [5]. *B) Witness coupon orientation, where the names denote material placement in the direction of cartesian directions*

Specimens were manufactured on an Aconity MIDI+ (Aconity3D GmbH, Germany) equipped with an Aerosint SPD v1 (Aerosint SA, Belgium), with a single mode fiber laser at a continuous wavelength of 1070 nm and spot size of 80 um. Due to the dissimilar thermal continuity and optical absorption of IR light between Bronze and 904L SS, different process parameters were selected for each material as detailed in Table 1. The interlayer rotation is 67 degrees for the 3-pt bending specimens, and 90 degrees for the witness coupons. The chamber was flushed with argon gas, and low O2 concentrations were maintained below 500 ppm throughout the entire process.

Table 1: Process Parameters by Material

Material	Power [W]	Scanning Speed [mm/s]	Hatch Spacing [μm]	Layer Thickness [μm]
CuSn10	200	500	120	40
904L SS	250	750	80	40

Scanning electron microscopy (SEM) was conducted on both powders at an operating voltage and current of 5kV and 0.10 mA at a working distance of 10.1 mm. Imaging of both powders was consistent with spherical powder, shown in Figure 2. Particle size distribution (PSD) characterization (Mastersizer 3000, Malvern Panalytical, UK) on both powders yielded a 10-90% percentile range of 18.7-46.1 μm for 904L stainless steel powder (Thyssenkrupp Materials Trading GmbH, Germany) and 6.01-33.4 μm for CuSn10 (Eckart TLS GmbH, Germany), averaged across 6 measurements taken for each material. The average volume powder size distribution is presented in Figure 2 as a percent volume density.

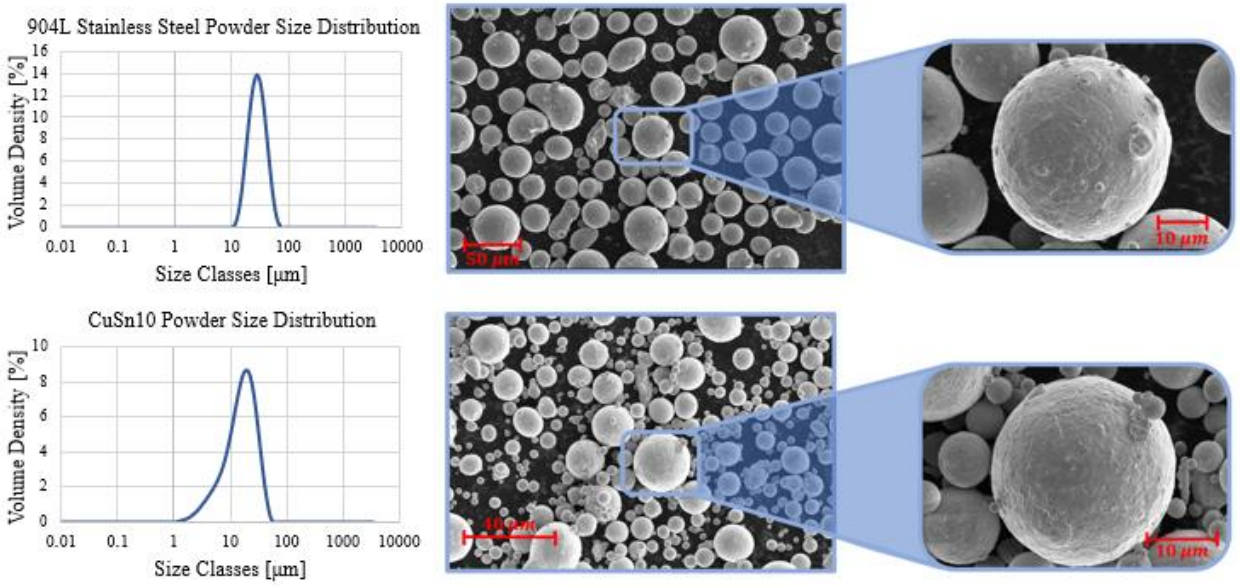

Figure 2: PSD for Bronze and 904L Stainless steel (left); SEM imaging of powder shape (right).

Morphological Analysis

Micro-computed tomography (micro-CT) was performed on all four witness coupons to evaluate the quality and internal defects of the as-built parts. All scans were completed with voxel size of 25 μm (pheonix v|tome|xL, Waygate Technologies, NY, USA). Scans results were converted to 8-bit .tiff images through ImageJ and imported into the Avizo (version 2022.1, Amira-Avizo, FEI, Thermo Fisher Scientific, USA) software for analysis and imaging.

Simulation Methods

Inherent strain is a product of thermal build-up due to laser energy input and is largely a factor of material properties (thermal and mechanical) and laser parameters. For single material builds,

inherent strain is often obtained from experimentation and coupled with simulation for additional insight as to the thermal or stress fields across layers or cross sections. To simulate the process of sintering dissimilar materials along the build direction, the bottom half of the witness coupon was designed pre-sintered into the build plate and the top half of was simulated as the sintered component. Within Ansys, the build plate and printed component can be assigned as having differing material properties. The inherent strain method is a physics-based simulation model capable of predicting residual stresses and strains of components and is a commercially available software among others capable of simulating thermomechanical build up in LPBF [6]. Because of this, it is only accurate to consider the simulated induced strain at the fusion plane to examine material interactions, and across the upper material section.

Numerical modeling and analysis were conducted over the AM LPBF Inherent Strain module in the Ansys Additive Print (AAP) module (Ansys, Inc. 2023) to establish the relationship between LPBF process parameters and the equivalent von-Mises stress and distortion in the as-built part using a finite element method. The build plate and printed component were generated within the Ansys Space Claim module. Cartesian elements of voxel size 1 mm were chosen for meshing the printed component, and tetrahedral elements of size 1 mm were chosen for the base plate. Material data for the 904L SS and CuSn10 was taken from JMatPro, a practical software for material properties. JMatPro's ability to calculate thermophysical and mechanical properties across a wide range of materials has been well documented. [7]–[9]

Results

Simulation Results

The inherent strain method within Ansys allows for the visualization of predicted regions which suffer from localized and global deformations and residual strain which may lead to build failure or unreliable mechanical behavior [10]. Table 2 summarizes maximum deformation, strain and stress for both witness coupons. It is important to note that all maximum values were found in regions adjacent to the fusion plane.

Table 2: Ansys Additive Print LPBF Inherent Strain Simulation Results

Material Orientation	Max. Deformation [mm]	Max. Equivalent Plastic Strain [%]	Max. Principal Strain [%]	Equivalent (von-Mises) Stress [MPa]
$(Br, SS)_Z$	0.0151	0.215	0.163	208.09
$(SS, Br)_Z$	0.0242	0.525	0.142	184.81

The simulations have produced contour maps which provide valuable insights into the local distributions of stress-strain-deformation. Figures 3 and 4 show the stress contour map obtained from the inherent strain simulation and highlights regions of high stress concentrations. The contour plot reveals the localized high-stress regions to be along the fusion plane between the two materials, indicating the presence of potential defect initiation sites.

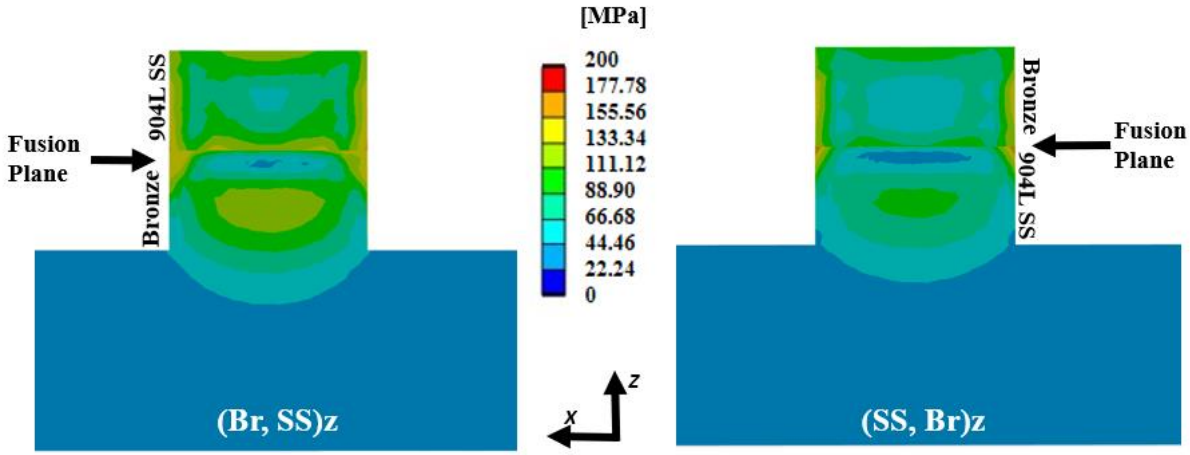

Figure 3: Equivalent (von-Mises) Stress [MPa] contour plots in a cross-sectional view along the XZ-plane for witness coupon $(Br, SS)_Z$ (left) and witness coupons $(SS, Br)_Z$ (right).

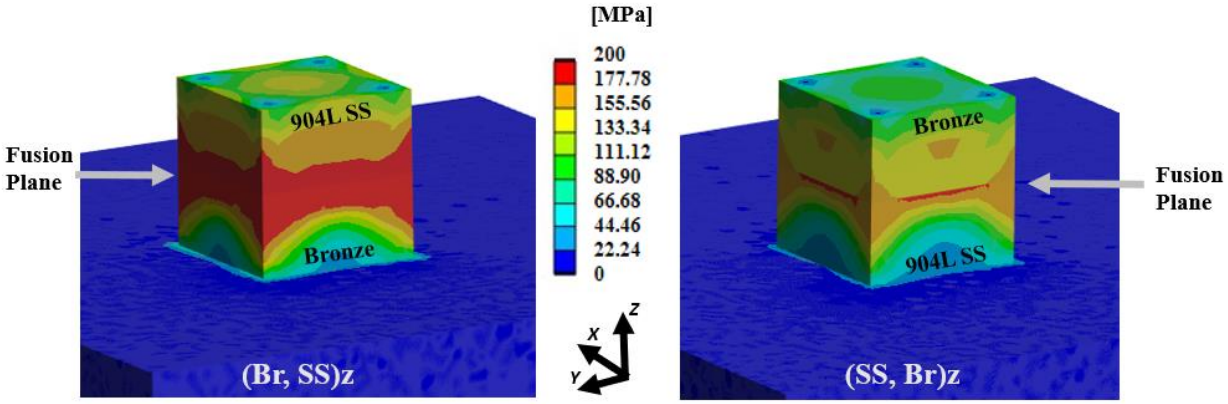

Figure 4: Equivalent (von-Mises) Stress [MPa] contour plots in an isometric for witness coupon $(Br, SS)_Z$ (left) and witness coupons $(SS, Br)_Z$ (right).

Figures 5 and 6 display the principal strain contour map. Similar to the stress contour map, strain analysis reveals pronounced strain concentrations along the fusion interface, suggesting regions prone to defect formation.

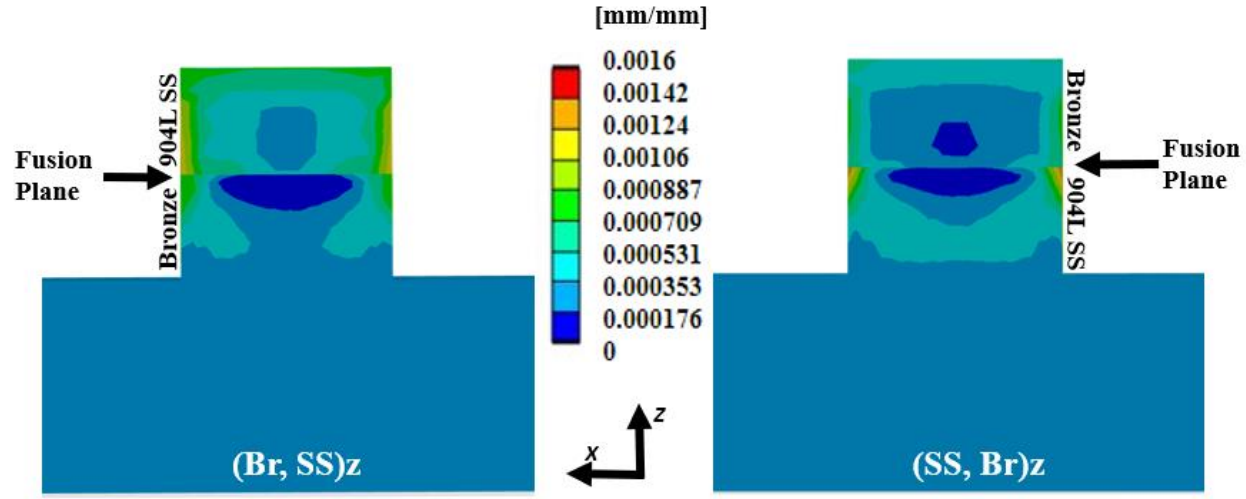

Figure 5: Maximum principal strain [mm/mm] contour plots in a cross-sectional view along the XZ-plane for witness coupon $(Br, SS)_Z$ (left) and witness coupons $(SS, Br)_Z$ (right).

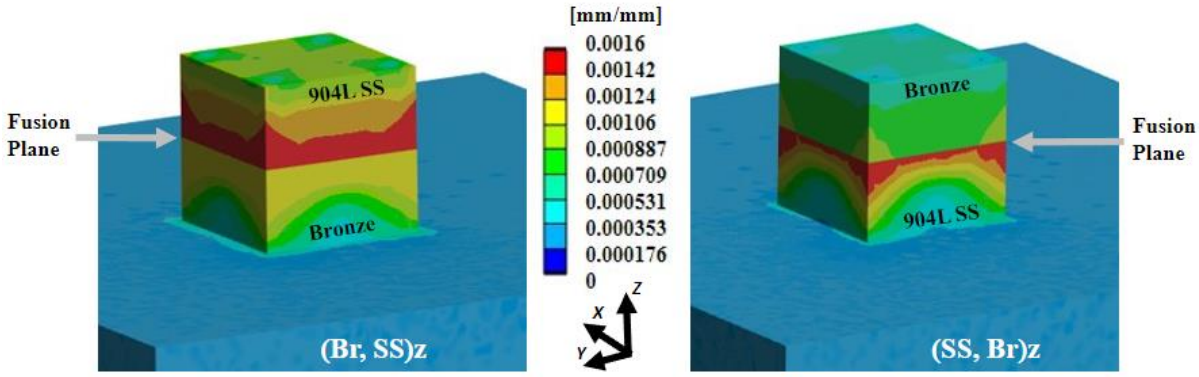

Figure 6: Maximum principal strain [mm/mm] contour plots in an isometric for witness coupon $(Br, SS)_Z$ (left) and witness coupons $(SS, Br)_Z$ (right).

Figures 7 and 8 display the displacement contour plots for either witness coupon. In this instance. It is important to note that while the $(Br, SS)_Z$ witness coupon is under more stress-strain, $(SS, Br)_Z$ appears to have experienced greater deformation. The difference in deformation between the two coupons is attributed to a dissimilarity in ductility between the materials used.

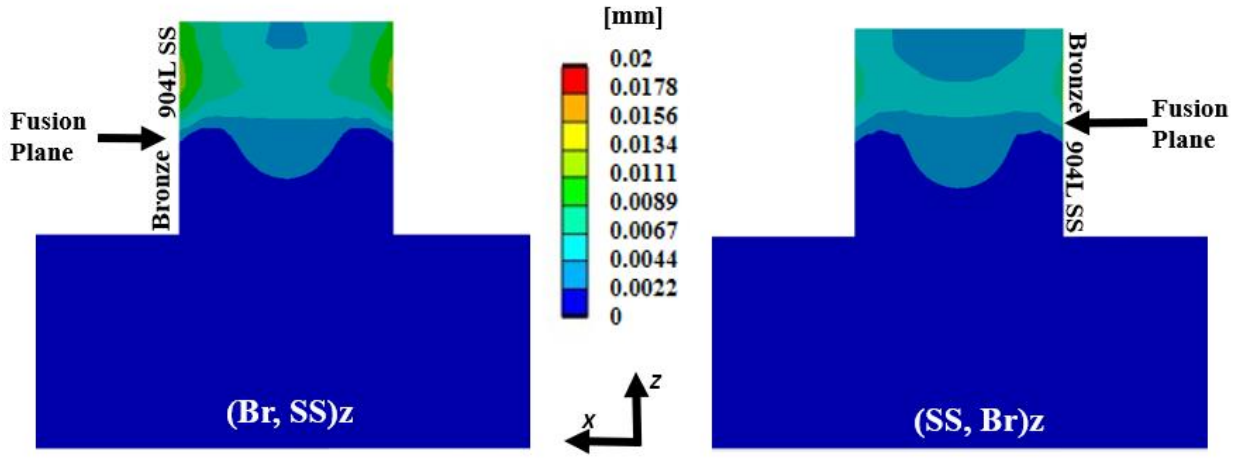

Figure 7: Maximum Deformation [mm] contour plots in a cross-sectional view along the XZ-plane for witness coupon (Br, SS)$_Z$ (left) and witness coupons (SS, Br)$_Z$ (right).

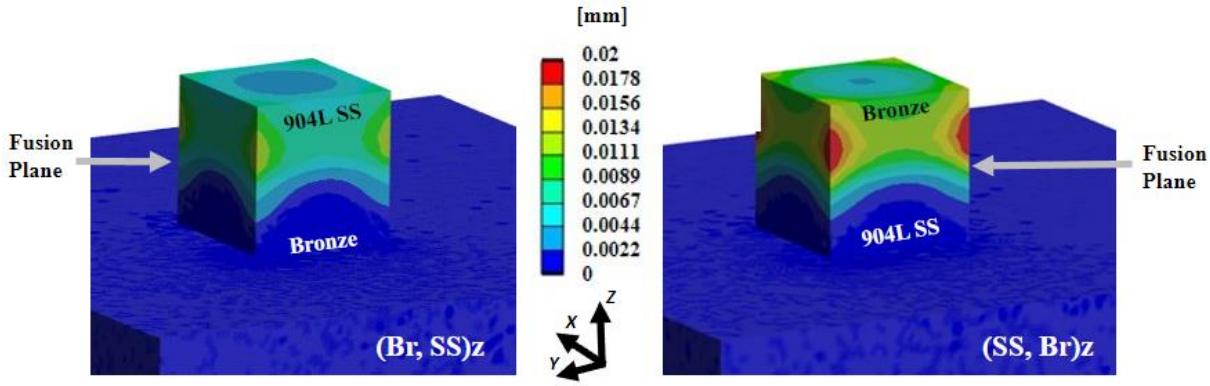

Figure 8: Maximum Deformation [mm] contour plots in an isometric for witness coupon (Br, SS)$_Z$ (left) and witness coupons (SS, Br)$_Z$ (right).

Morphological Results

Micro-CT imaging was performed on the as-built witness coupons to examine characteristics of interest and defects which may help determine the influence of build orientation on MM-LPBF part quality. Figure 9 presents a cross-sectional micro-CT image of both witness coupons, showcasing various types of defects observed within the printed part. Cracks, voids and porosities are self-evident in the micro-CT image of (Br, SS)$_Z$.

The micro-CT image analysis reveals a notable difference in the defect characteristics between the two material orientations, which is consistent with what is seen in the simulation contour maps. Figure 9B and 9D presents a micro-CT image of steel sintered on top of bronze. In this configuration, cracking appears to be propagated further along the fusion plane and into the witness coupon. In contrast, Figures 9A and 9B have a noticeably lower density of defects with no visible cracking at this voxel size. This difference in defect density can be attributed to dissimilar thermal expansion coefficients which may lead to increased thermal gradients at the interface, promoting crack formation. Interestingly, coupon (Br, SS)$_Z$ did exhibit visual deformation, as noted by the

blue dotted line across the fusion plane in Figure 9C. In this orientation, it appears that the edges of the coupon deformed upwards during the first half of the print causing a crescent-shaped cross section. This is likely a result of a higher rate of thermal dissipation at the edges of the print.

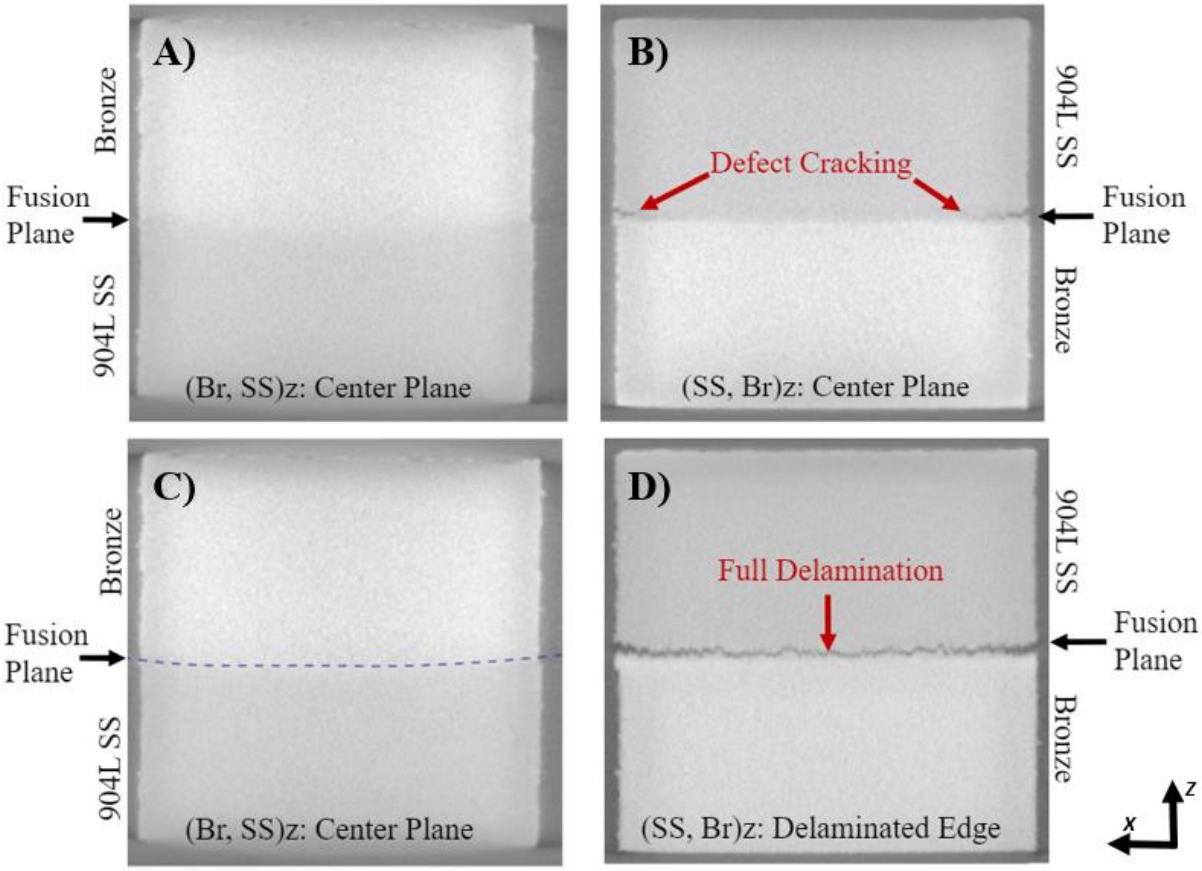

Figure 9: Micro-CT scans in a cross-sectional view along the XZ-plane. A) Center plane scan of $(Br, SS)_Z$, B) Center plane scan of $(SS, Br)_Z$ C) Center plane scan of $(Br, SS)_Z$ showing apparent curvature of the fusion plane D) Edge scan of $(SS, Br)_Z$ showing complete delamination at the edge of the fusion plane.

Discussion

Thermally Induced Defects

In this study, we focused on the examination of defects found in micro-CT scans and thermally induced strain simulations along the fusion plane between two dissimilar materials sintered along the build direction through MM-LPBF. The aim is to identify whether material arrangement along the build direction, or part orientation, should be considered as an influencing factor for defect mitigation. Thermally induced strain simulations help shed light on the underlying mechanisms responsible for crack formation for this process.

Results reveal several significant similarities between the defects identified in micro-CT scans and the stress and strain distributions. Both the experimental and simulated analyses consistently

indicate crack initiation and propagation along the fusion plane. This observation strongly suggests that the fusion zone acts as a preferential site for crack formation, which aligns with previous studies reporting fusion-related defects as a common occurrence in multi-material LPBF-printed parts [11], [12]. Furthermore, the similarities in crack orientations between the micro-CT scans and simulations highlight the influence of process-induced thermal gradients and residual stresses on crack propagation. The simulations accurately capture the anisotropic nature of LPBF processes and demonstrate how the directionality of thermal gradients and residual stresses contributes to the preferential alignment of cracks parallel to the fusion plane. These findings emphasize the importance of considering thermal history and residual stress states in predicting and mitigating crack formation in LPBF-produced components.

The contrasting thermal expansion coefficients of stainless steel and bronze play a crucial role in crack formation. Stainless steel has a lower coefficient of thermal expansion compared to bronze. During heating and cooling cycles associated with layer-by-layer metal AM, the stainless steel is expected to expand and contract much less than the underlying bronze, in the case of stainless steel being sintered on top of bronze [13], [14]. These dissimilar expansion and contraction rates create substantial thermal stresses at the fusion plane. Due to the higher laser energy input for steel required for its high solidification temperature (mainly caused by the large difference in hatch spacing in this instance), the first few steel layers in $(Br, SS)_Z$ would exude a much greater thermal load on the bronze below as the bronze is re-melted underneath the steel powder. This may cause undue thermal expansion at the fusion plane, and cause the steel adjacent to the interface to experience high strain loads that it not seen in the opposite material orientation as exhibited in Figure 6. In this case, the thermally induced strain produced residual stresses which exceeded the material's yield strength, causing failure to occur through cracking as observed in the micro-CT results in Figure 9.

The high solidification temperature of steel exacerbates this phenomenon as well. Because the steel layer solidifies at a higher temperature, cooling time for the steel will be greater compared to the bronze substrate. As a result, uneven component cooling and solidification shrinkage are expected to have occurred between the materials. This non-uniform cooling and solidification shrinkage may introduce additional stress concentrations at the fusion plane and act as preferential sites for crack initiation [15].

Taken together, the contrasting thermal expansion coefficients and solidification behavior of stainless steel and bronze in LPBF contribute to the formation of cracks. Understanding these mechanisms is crucial for devising strategies to minimize cracks and enhance the quality and reliability of MM- LPBF components. Overall, the similarities between the defects found in micro-CT scans and the stress and strain distributions obtained from thermomechanical simulations have provided valuable insight into the underlying mechanisms governing crack formation in LPBF-produced components. This knowledge can inform future development of improved process parameters, optimized support structures, and post-processing treatments to mitigate crack formation and enhance the overall mechanical integrity of LPBF-printed parts.

Effects of Intermetallic Formation

In addition to the factors discussed above, another potential cause for the formation of cracks in the fusion zone between 904L stainless steel and bronze could be the formation of intermetallic compounds. When dissimilar metals are sintered together, there is a possibility of interdiffusion of

alloys within the melt zone at the fusion plate and subsequent intermetallic formation at the interface. Intermetallics, FeSn2 for example, would be expected to form in the presence of these two alloys [16]. These intermetallic compounds can exhibit different or unpredictable thermophysical and mechanical properties but are generally known for being more brittle than their constituent materials, potentially creating localized stress concentrations and crack initiation sites [17]. Therefore, the presence and characteristics of intermetallic phases should be considered as a potential contributor to crack formation and should be investigated further through microstructural analysis techniques such as energy dispersive spectroscopy (EDS) to affirm the chemical composition near the fusion plane. Understanding the role of intermetallic formation in crack initiation and propagation will aid in developing strategies to control their formation and mitigate crack-related defects in LPBF processes involving dissimilar metal combinations.

It is important to note that this study focused on a specific set of materials and process parameters, and further investigations are necessary to generalize these findings to other material combinations. Additionally, the limitations associated with the resolution of micro-CT scans and the assumptions made in the thermomechanical simulations should be considered in future studies to enhance the accuracy and reliability of the results.

Methods for reducing thermally induced stresses

The thermally induced stresses caused at the fusion zone between two materials could be mitigated by devising scanning strategies that account for the differing thermal properties of the materials. To achieve this, thermal or thermomechanical models that capture these differences must be used to generate the scan strategies. One example of such a strategy is SmartScan [18]where a thermal model is utilized to generate laser scan sequences that maintain thermal uniformity across a part during printing using a single material. For multi-material printing, it is not sufficient to have thermal uniformity because of the impact of differing coefficients of thermal expansion between the materials. A potential approach is to generate scan strategies that achieve uniform thermal expansion across the part, particularly near the fusion zone. Such a method could be further enhanced by leveraging multi-laser LPBF systems, which provide additional degrees of freedom to design scan strategies that can reduce thermal gradients and defects [19].

Acknowledgements

The authors would like to gratefully acknowledge Dr. Kenneth Meinert of the Applied Research Laboratory at Pennsylvania State University for assistance with conducting the micro-CT scans, and Dr. Matthew Dantin of Naval Surface Warfare Center Carderock Division (NSWCCD) for his contributions towards the training and theoretical background of thermophysical simulation.

References

[1] S. Qu, J. Ding, J. Fu, M. Fu, B. Zhang, and X. Song, "High-precision laser powder bed fusion processing of pure copper," *Addit Manuf*, vol. 48, no. PA, p. 102417, 2021, doi: 10.1016/j.addma.2021.102417.

[2] J. Chen, Y. Yang, C. Song, M. Zhang, S. Wu, and D. Wang, "Interfacial microstructure and mechanical properties of 316L /CuSn10 multi-material bimetallic structure fabricated by selective laser melting," *Materials Science and Engineering A*, vol. 752, no. March, pp. 75–85, 2019, doi: 10.1016/j.msea.2019.02.097.

[3] C. Tan, K. Zhou, W. Ma, and L. Min, "Interfacial characteristic and mechanical performance of maraging steel-copper functional bimetal produced by selective laser melting based hybrid manufacture," *Mater Des*, vol. 155, pp. 77–85, 2018, doi: 10.1016/j.matdes.2018.05.064.

[4] J. Chen, Y. Yang, C. Song, D. Wang, S. Wu, and M. Zhang, "Influence mechanism of process parameters on the interfacial characterization of selective laser melting 316L/CuSn10," *Materials Science and Engineering A*, vol. 792, no. March, p. 139316, 2020, doi: 10.1016/j.msea.2020.139316.

[5] "Aerosint, Desktop Metal Company 'Unlocking Multi-Material Additive Manufacturing.'" 2022.

[6] J. S, R. M, S. P. AVS, N. B K, and C. U, "Study of residual stresses and distortions from the Ti6Al4V based thin-walled geometries built using LPBF process," *Defence Technology*, no. xxxx, pp. 1–9, 2023, doi: 10.1016/j.dt.2023.01.002.

[7] Z. Guo, N. Saunders, A. P. Miodownik, and J.-P. Schillé, "Modelling of materials properties and behaviour critical to casting simulation," *Materials Science and Engineering: A*, vol. 413, pp. 465–469, Dec. 2005, doi: 10.1016/j.msea.2005.09.036.

[8] Z. Guo, N. Saunders, J. P. Schillé, and A. P. Miodownik, "Material properties for process simulation," *Materials Science and Engineering A*, vol. 499, no. 1–2, pp. 7–13, 2009, doi: 10.1016/j.msea.2007.09.097.

[9] N. Saunders, Z. Guo, X. Li, A. P. Miodownik, and J. P. Schillé, "Using JMatPro to model materials properties and behavior," *Jom*, vol. 55, no. 12, pp. 60–65, 2003, doi: 10.1007/s11837-003-0013-2.

[10] H. Mohammadtaheri, R. Sedaghati, and M. Molavi-Zarandi, "Inherent strain approach to estimate residual stress and deformation in the laser powder bed fusion process for metal additive manufacturing—a state-of-the-art review," *International Journal of Advanced Manufacturing Technology*, vol. 122, no. 5–6, pp. 2187–2202, 2022, doi: 10.1007/s00170-022-10052-2.

[11] J. Schanz *et al.*, "Individual process development of single and multi-material laser melting in novel modular laser powder bed fusion system," *Progress in Additive Manufacturing*, vol. 7, no. 3, pp. 481–493, 2022, doi: 10.1007/s40964-022-00276-9.

[12] M. Mehrpouya, D. Tuma, T. Vaneker, M. Afrasiabi, M. Bambach, and I. Gibson, "Multimaterial powder bed fusion techniques," *Rapid Prototyp J*, vol. 28, no. 11, pp. 1–19, 2022, doi: 10.1108/RPJ-01-2022-0014.

[13] A. V. Gusarov, M. Pavlov, and I. Smurov, “Residual stresses at laser surface remelting and additive manufacturing,” *Phys Procedia*, vol. 12, no. PART 1, pp. 248–254, 2011, doi: 10.1016/j.phpro.2011.03.032.

[14] H. E. Sabzi *et al.*, “Grain refinement in laser powder bed fusion: The influence of dynamic recrystallization and recovery,” *Mater Des*, vol. 196, no. October, p. 109181, 2020, doi: 10.1016/j.matdes.2020.109181.

[15] N. C. Levkulich, S. L. Semiatin, J. E. Gockel, J. R. Middendorf, A. T. DeWald, and N. W. Klingbeil, “The effect of process parameters on residual stress evolution and distortion in the laser powder bed fusion of Ti-6Al-4V,” *Addit Manuf*, vol. 28, no. January, pp. 475–484, 2019, doi: 10.1016/j.addma.2019.05.015.

[16] M. J. L. Gines, G. J. Benítez, W. Egli, J. L. Zubimendi, and T. Pérez, “Formation of an Fe-Sn Intermetallic Layer during the Reflow Process after Tin Plating,” *Plating and Surface Finishing*, vol. 90, no. 10, pp. 44–49, 2003.

[17] M. Armbrüster and Y. Grin, “Catalytic Materials Based on Intermetallic Compounds,” in *Reference Module in Chemistry, Molecular Sciences and Chemical Engineering*, 2014. doi: 10.1016/B978-0-12-409547-2.11227-2.

[18] K. S. Ramani, C. He, Y. L. Tsai, and C. E. Okwudire, “SmartScan: An intelligent scanning approach for uniform thermal distribution, reduced residual stresses and deformations in PBF additive manufacturing,” *Addit Manuf*, vol. 52, no. October 2021, p. 102643, 2022, doi: 10.1016/j.addma.2022.102643.

[19] C. He, K. Ramani, and C. Okwudire, “An intelligent Scanning Strategy (SmartScan) for Improved Part Quality in Multi-Laser PBD Additive Manufacturing,” *Addit Manuf*, no. 23, 2022.